AGU PUBLICATIONS

Geophysical Research Letters

RESEARCH LETTER
10.1002/2015GL065195

**Key Points:**
- The flat slab follows the shape of the continental Moho due to the interplate suction force
- The dehydration and ecologitization of the slab is delayed by flat subduction
- Molten rocks and Brazilian Shield are imaged in the crust of Western and Eastern Cordillera

**Supporting Information:**
- Texts S1 and S2, Figures S1–S6, and Table S1

**Correspondence to:**
Y. Ma,
yrma@caltech.edu

**Citation:**
Ma, Y., and R. W. Clayton (2015), Flat slab deformation caused by interplate suction force, *Geophys. Res. Lett.*, *42*, 7064–7072, doi:10.1002/2015GL065195.

Received 1 JUL 2015
Accepted 17 AUG 2015
Accepted article online 20 AUG 2015
Published online 12 SEP 2015



# Flat slab deformation caused by interplate suction force

**Yiran Ma[1] and Robert W. Clayton[1]**

[1]Seismological Laboratory, California Institute of Technology, Pasadena, California, USA

**Abstract** We image the structure at the southern end of the Peruvian flat subduction zone, using receiver function and surface wave methods. The Nazca slab subducts to ~100 km depth and then remains flat for ~300 km distance before it resumes the dipping subduction. The flat slab closely follows the topography of the continental Moho above, indicating a strong suction force between the slab and the overriding plate. A high-velocity mantle wedge exists above the initial half of the flat slab, and the velocity resumes to normal values before the slab steepens again, indicating the resumption of dehydration and ecologitization. Two prominent midcrust structures are revealed in the 70 km thick crust under the Central Andes: molten rocks beneath the Western Cordillera and the underthrusting Brazilian Shield beneath the Eastern Cordillera.

## 1. Introduction

The subduction zone along South America includes the longest (along strike) flat slab on Earth (see Figure 1 in *Skinner and Clayton* [2013]). The Peruvian flat slab, which spans over 1500 km long as indicated by a gap in the arc volcanoes [*Ramos and Folguera*, 2009], is especially interesting for investigating the dynamic buoyancy that has flattened the slab. It appears to be tied to the Nazca Ridge, which has migrated southward along the trench from 11°S at the point of initial subduction (at ~11.2 Ma) [*Hampel*, 2002]. Its present location coincides with the southern end of the flat subduction segment. Recent studies indicate that the slab subducts at an 18° angle to about 100 km depth and remains flat for about 300 km before resuming its descent [*Hayes et al*., 2012; *Phillips and Clayton*, 2014]. Based on the arc volcanoes, various segments of the subduction zone of South America have also experienced flat subduction episodes in the past [*Mamani et al*., 2010; *Ramos and Folguera*, 2009; *Trumbull et al*., 2006]. In particular, in Oligocene there was a flat slab beneath the Altiplano plateau that is immediately to the south of the present flat subduction zone considered here [*Mamani et al*., 2010; *O'Driscoll et al*., 2012; *Ramos and Folguera*, 2009].

The mechanism that transforms a normal-dipping slab into the flat geometry is not clear. The correlation between flat subduction and the subducting anomalies on the oceanic floor (e.g., Nazca Ridge in Figure 1, and J. Fernandez Ridge for Pampean flat subduction near Chile) suggests that buoyancy provided by the subducted oceanic ridge/plateau causes the flat subduction [*Gutscher*, 2002]. The onset of the Peruvian flat subduction is coincident with the subduction of the Nazca Ridge [*Hampel*, 2002; *Skinner and Clayton*, 2013], but this correlation does not work for all flat slab episodes [*Skinner and Clayton*, 2013]. Moreover, the buoyancy solely provided by thickened oceanic crust is not sufficient [*Gerya et al*., 2009] and is not as significant compared with the lifting force related to upper plate motion and upper mantle viscosity [*van Hunen et al*., 2002, 2004]. Therefore, other factors such as the enhanced mantle wedge suction by a thick continental craton near the subduction zone are also suggested to be significant in flattening the slab in South America [*Manea et al*., 2012; *O'Driscoll et al*., 2012]. The change in distance to the cratonic root, which controls the interplate suction force, is suggested to have caused the flatten and resteepen of the Oligocene flat slab beneath the Altiplano [*O'Driscoll et al*., 2012].

Distinguishing between the structure of flat and normal subduction zones is important for understanding the mechanisms as well as consequences of the flat subduction. With the recent deployments of seismic arrays, several studies have emerged on the structure in southern Peru where the slab transitions from normal subduction in the southeast to flat subduction in the northwest [*Dougherty and Clayton*, 2014; *Ma and Clayton*, 2014; *Phillips and Clayton*, 2014; *Phillips et al*., 2012]. The flat subduction zone structure to the north is being investigated by several studies [*Antonijevic et al*., 2015; *Bishop et al*., 2013; *Eakin et al*., 2015].

In this study, we focus on the southernmost Peruvian flat subduction zone, through detailed images of the structures of the oceanic Moho (slab), the continental Moho, and midcrust structures obtained with receiver function and surface wave tomography methods. In particular, we show that the shape of the flat

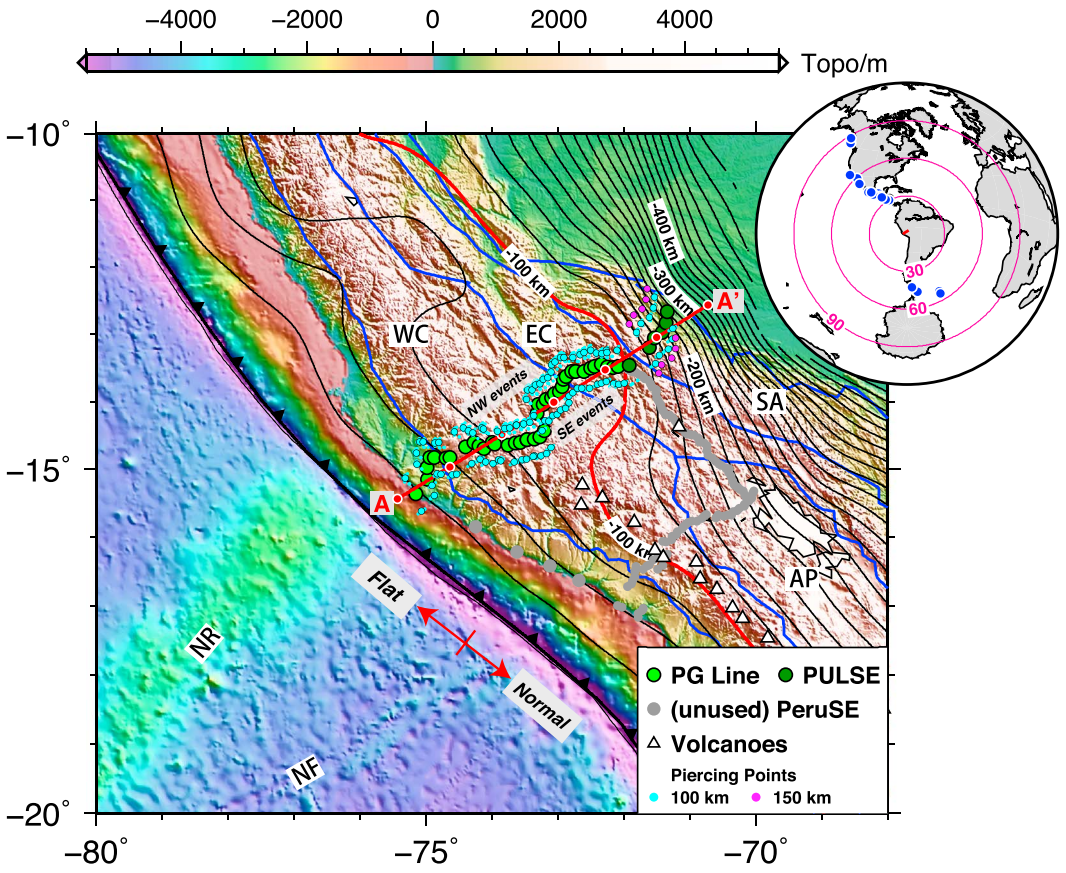


**Figure 1.** Location of the seismic stations (green dots) used in this study. The grey dots are stations of PeruSE experiment that are not used. A-A' is the projection line of the stations, with 100 km intervals marked with red dots. The main units building the Central Andes are delineated with blue lines (modified from *Oncken et al.* [2006] and *Tassara* [2005]). WC: Western Cordillera; EC: Eastern Cordillera; AP: Altiplano Plateau; and SA: Sub-Andean Ranges. The Holocene volcanoes are denoted with white triangles (data from http://www.volcano.si.edu/world). The seafloor features are the Nazca Ridge (NR) and the Nazca Fracture Zone (NF). Slab contours (data from http://earthquake.usgs.gov/data/slab) are plotted at 25 km intervals. The 100 km depth slab contour is highlighted with a thick red line, which shows the change of the slab geometry. The top right insert figure shows the teleseismic events used in the receiver function study. The piercing points at 100 km depth are shown in cyan dots in the map, falling into NW and SE events groups. For each station, the centers of the two groups of piercing points are also shown in cyan dots (with black edge). For PULSE stations, we also show piercing points at 150 km depth as pink dots.

slab correlates with the topography of the Moho, which shows the importance of the interplate suction force in the development of flat subduction. Also, a better velocity model is obtained from the surface wave inversion by using velocity discontinuities controlled by the receiver functions. A lateral velocity contrast in the mantle wedge that was first shown in *Ma and Clayton* [2014] is evidence of a delayed dehydration of the flat slab.

## 2. Data and Results

The data we use are primarily from a dense line of seismic stations (PG line) above the flat subduction regime, which is part of a box-like array (PeruSE) in southern Peru [*PeruSE*, 2013]. This line includes 40 stations, and was operational from November 2010 to March 2013. We also use six stations (FS stations) from the PULSE experiment [*Bishop et al.*, 2013; *Eakin et al.*, 2014]. The array has an interstation spacing of approximately 10 km and spans from the coast to the sub-Andean region, where the flat slab resumes a normal-dipping geometry (Figure 1).

### 2.1. *Ps* Receiver Functions

We use iterative time-domain deconvolution [*Kikuchi and Kanamori*, 1982; *Ligorría and Ammon*, 1999] to retrieve P-to-S receiver functions (RFs). A low-pass Gaussian filter is applied with a parameter of 1.5 (the corresponding

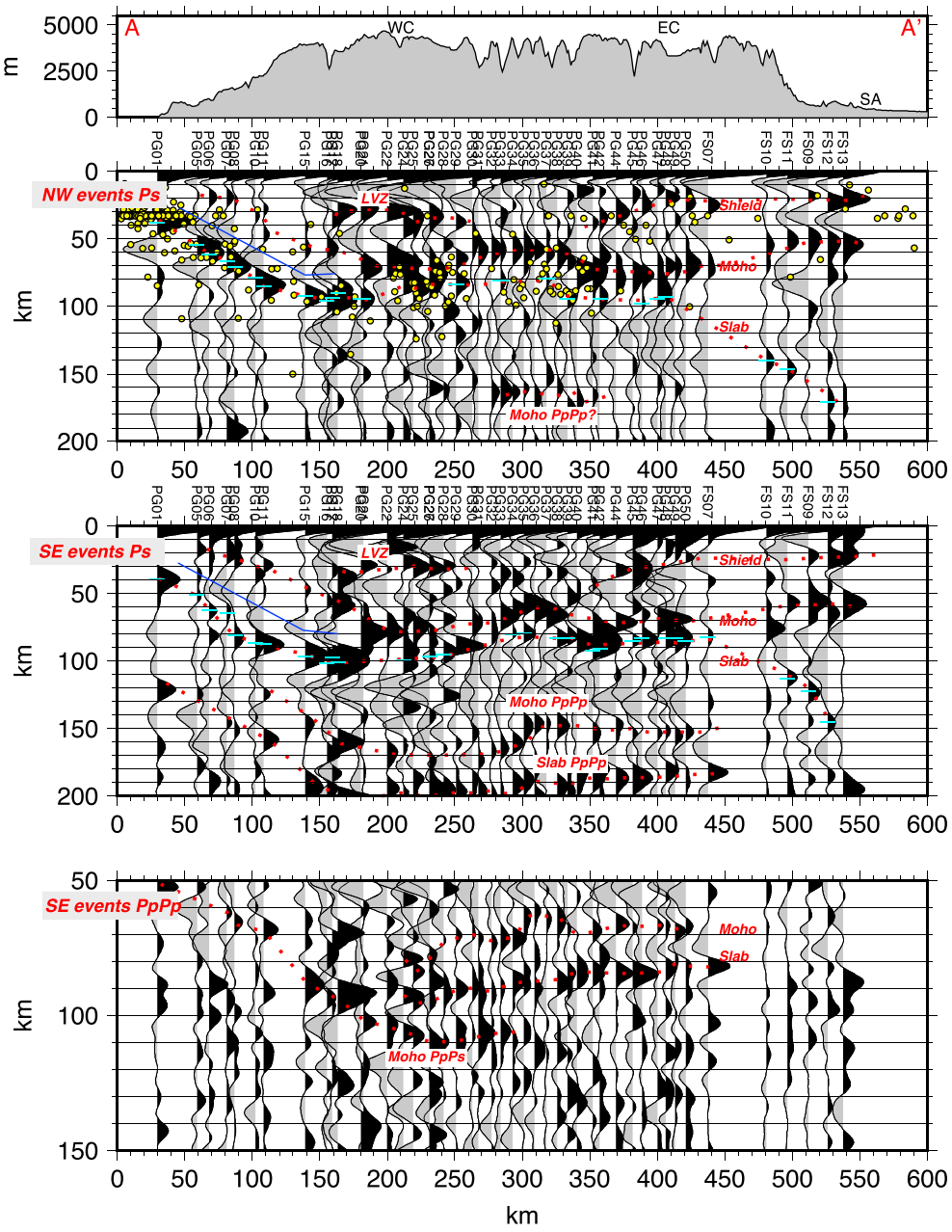


**Figure 2.** Stacked RFs for each station projected along A-A′ profile (Figure 1). Events from NW and SE back azimuths are plotted in separate panels. First and second panels are for *Ps* RFs. Third panel is for *PpPp* RFs (see texts for details). The yellow dots are earthquakes from the National Earthquake Information Center catalog (from 1980 to November 2014), with magnitude not less than 4, and within ±60 km from the profile. The density of the seismicity is better illustrated in Figure S4, which shows two clusters centered at 225 and 325 km distance. The red dotted lines delineate the speculated structures. The negative signals corresponding to the conversion at the top of the slab are marked with blue lines. The cyan dashes are picked slab depths shown in Figure 3b.

cutoff frequency and the pulse width in time domain are approximately 0.7 Hz and 1.36 s, respectively). Figure 1 shows the events used, all of which have a magnitude larger than 5.9 and an epicentral distance in the range of 29–86° (Table S1 in the supporting information). The events are dominantly from NW and SE azimuths, and accordingly their piercing points are separated into two groups as shown in Figure 1. Since there are noticeable along-strike variations in the structure, we show the RFs from the stack of the two groups of events separately in Figure 2. Before the stacking, the IASP91 model [*Kennett and Engdahl*, 1991] is used as the reference to transform the time axis of the RFs (Figure S1) to depth, using the depth-time relation for the *Ps* phase. Since the

events are coming from the along-strike direction, we did not apply any correction for the dipping slab. In Figure 2, we show the converted phases associated with the Moho, slab, and the midcrustal structures.

The Moho is ~70 km deep beneath the Western and Eastern Cordillera and rises to ~60 km in the region between the two. The Moho signal is much weaker in the forearc region, indicating a smaller velocity contrast between the uppermost mantle and the crust. In the midcrust beneath the Western Cordillera, there are strong positive and negative signals, which indicate the bottom and the top of a low-velocity zone (LVZ), respectively. Beneath Eastern Cordillera and sub-Andean region, we observe a strong positive signal with an inclined geometry that coincides with increased crustal seismicity. We interpreted it as the top interface of the underthrusting Brazilian Shield, whose existence beneath the Eastern Cordillera is widely recognized [*Lamb et al*., 1996; *McQuarrie et al*., 2005; *Phillips and Clayton*, 2014; *Phillips et al*., 2012].

In the NW events profile (Figure 2), the slab signals (the *Ps* conversion at the oceanic Moho) are strong from the coast (PG01) to the initial 50 km of the flattened slab (PG15-PG21) at 95 km depth. The positive signals are then contaminated by strong negative multiples from the midcrust LVZ beneath stations PG22–PG27 (200–230 km distance range in A-A'). Further inland, the flat slab signal does not appear continuously at every station and we pick the slab signal according to its lateral consistency among stations and the seismicity shown by the yellow dots. In the SE events profile, the flat slab signal is more continuous. The flat slab starts at ~100 km depth and shallows to ~80 km depth inland. This trend is magnified with the slab multiples (*PpPp*) which will be discussed in the following section. Further inland, the resteepened slab imaged by the SE events is ~30 km shallower compared to the NW events profile due to the different geometry of the slab sampled by the two azimuths (see piercing points at 150 km depth in Figure 1).

The depth of the Moho can be controlled to some degree by the *Vp/Vs* ratio used for the time to depth conversion, with the relationship being approximately $\Delta H = -74.3\ \Delta(Vp/Vs)$ (see Text S1 for details), where *Vp/Vs* is the average for the entire ~60 km thick crust. However, we will see that the observed lateral variations in the Moho geometry cannot be accounted by the *Vp/Vs* ratio. Since we do not observe any anomalous crustal structure above the up-bulged Moho, we may assume the crustal *Vp/Vs* there to be 1.75, an average value from previous study [*Phillips and Clayton*, 2014]. To eliminate the bulge in the Moho would require *Vp/Vs* to be ~1.88 for the Eastern Cordillera, and ~1.88/2.0 (larger in SE events profile) for the Western Cordillera. These values are extreme and disagree with the observations on the *Vp/Vs* ratios in the study area [*Phillips and Clayton*, 2014; *Phillips et al*., 2012]. A decreasing *Vp/Vs* inland, in order to remove the shallowing trend in Moho/slab, is also not observed [*Phillips and Clayton*, 2014].

### 2.2. *PpPp* Receiver Functions

In addition to the standard *Ps* converted phase, we also observe a strong and positive *PpPp* phase in the SE events profile (Figures S1 and 2). Because the *P* wave reflection at the free surface changes polarity, the *PpPp* phase is generally negative in RFs for an interface with positive impedance contrast (downward) such as the Moho. However, with a dipping interface, it can be positive for the events coming from the downdip direction (e.g., *Linkimer et al*. [2010], see Text S2 for more details). This is the case with the SE events because the slab is dipping toward the SE direction near the transition from flat to normal subduction (Figure 1). The dip angle is evident in the cross sections of seismicity parallel to the trench and is estimated to increase from ~10° at ~250 km from the trench to ~20° at ~450 km from the trench (Figure S4 of *Dougherty and Clayton* [2014]).

The *PpPp* image (also converted to depth with IASP91 model) clearly shows that the Moho and slab are shallowing inland, which is also evident in the *Ps* phase but more pronounced with *PpPp*. In addition, an up-bulged Moho is imaged at 310 km distance. An increase in dip angle or *P* wave velocity inland, for which we have no detailed models, could also cause an apparent shallowing. However, the similarities in depths and lateral changes in the interfaces between *Ps* and *PpPp* images give us the confidence that the IASP91 model [*Kennett and Engdahl*, 1991] we used is appropriate to do the time to depth conversion.

### 2.3. Shear Wave ($V_{SV}$) Velocity

We show the shear wave velocity ($V_{SV}$) structure along the same profile (A-A' in Figure 1) in Figure 3, which is determined from the Rayleigh wave dispersion curves (6–67 s period) retrieved from ambient noise and earthquake data that were previously reported in *Ma and Clayton* [2014]. In *Ma and Clayton* [2014], we inverted for smooth 1-D structures at each location inside of the box-like array from the dispersion curves using a reference

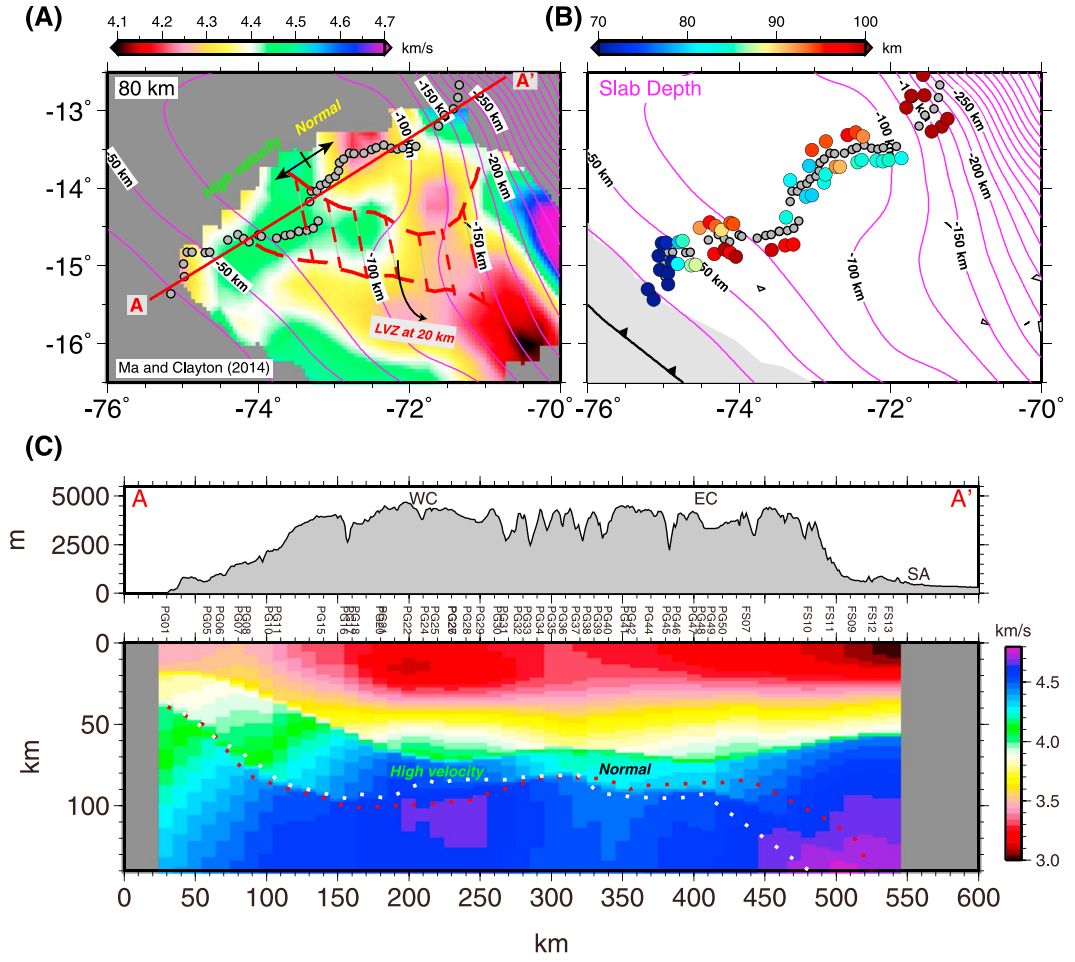


**Figure 3.** (a) The depth-slice of $V_{SV}$ structure at 80 km depth from *Ma and Clayton* [2014]. Note the contrast between the high and normal velocity mantle. We also plot the extent of the upper-midcrust low-velocity zone (LVZ) on top of it. The boundary of the LVZ is from the 3.2 km/s velocity contour in 20 km depth slice in *Ma and Clayton* [2014]. (b) Depth of the Nazca slab. The data points correspond to the cyan dashes in Figure 2. Pink contours are Slab1.0 model [*Hayes et al.*, 2012]. (c) Shear wave velocity structure inverted from Rayleigh wave dispersion (6–67 s period). The white and red dotted lines are the slab depths from RFs (NW and SE events, respectively) in Figure 2.

model without velocity discontinuities. To improve the velocity estimates along the array of stations used in this study, we use the depths of Moho and slab determined from the RFs (averaged from NW and SE events, and laterally smoothed). We add velocity discontinuities at the depths of the two interfaces in the initial model (Figure S5) and impose less damping across them during the inversion. The initial model is a simple three-layer model with $V_S$ of 3.5 km/s for the crust, 4.3 km/s for the mantle wedge, and 4.5 km/s below the mantle wedge (Figure S5). We discretize the model into 2 km fine layers above 200 km depth for the inversion, and the result is shown in Figure 3c. To confirm the pattern in the mantle, we also discretized the top 50 km of the crust into 2 km layers, while treating the rest of the crust, the mantle wedge, and the slab (assumed to be 80 km thick) as single layers (Figure S5b), and the result (Figure S6) is comparable to Figure 3c.

In the distance range of ~260–420 km (Figure 3), the mantle wedge shows a comparatively lower velocity distinct from the first half (150–260 km) of the flat slab segment, which is characterized by high velocity. The horizontal extent of this high-velocity mantle wedge is shown in Figure 3a, which is a depth slice at 80 km depth from *Ma and Clayton* [2014]. The low velocity may indicate the resumption of the dehydration of the slab before it resumes the normal-dipping subduction. The low velocity extends in depth through the entire oceanic lithosphere, which can be partly due to the smearing effect of the inversion. Alternatively, the oceanic lithosphere may indeed have a low-velocity upper mantle due to the formation of the Nazca ridge, whose subducted portion may cover a larger area than its onshore projection into our study area [*Hampel*, 2002].

## 3. Discussion

The results of the paper show that beneath the over 4 km high Central Andes, there are two prominent crustal features—the low-velocity zone beneath the Western Cordillera and the Brazilian Shield beneath the Eastern Cordillera. The Nazca slab is not uniformly flat and tends to follow the topography of the Moho.

### 3.1. The Andean Low-Velocity Zone

The low-velocity zone beneath the Western Cordillera is shown in both RFs and surface wave results (Figures 2 and 3c). The low-velocity zone is shown in 10–25 km depth range from surface wave (Figure 3c) and 15–30 km depth from RFs (Figure 2). The discrepancy may be due to that the *Vp*/*Vs* ratio used in migrating the RFs is smaller than reality [*Zhu and Kanamori*, 2000]. This zone was previously mapped in this region [*Ma and Clayton*, 2014]. It is oblique to the present trench (Figure 3a) and is suggested to be molten rocks related to the volcanism during the steepening of the Oligocene flat slab beneath the Altiplano plateau [*Ma and Clayton*, 2014]. This low-velocity zone, as part of the Andean low-velocity zone, widely exists in the crust of the Central Andes [*Schilling et al*., 2006; *Ward et al*., 2013; *Yuan et al*., 2000] and can be the channel for the crustal flow which is important in building the high and flat plateau [*Husson and Sempere*, 2003; *Yang et al*., 2003]. However, despite of the apparent large volume of the low-velocity zone, this does not indicate that the mantle-derived melts add significantly to thickening the crust. From the compositions of the ignimbrites, only minor andesitic melts (from the mantle) are thought to contribute to this low-velocity zone, while the melting of the crust itself is the dominant component [*Mamani et al*., 2010; *Schilling et al*., 2006].

### 3.2. The Brazilian Shield

The extent of the underthrusting Brazilian Shield beneath the Eastern Cordillera has previously been determined from the mantle structure [*Beck and Zandt*, 2002; *Dorbath et al*., 1993; *Myers et al*., 1998]. Recently, *Phillips et al*. [2012] and *Phillips and Clayton* [2014] have imaged the top of it as positive receiver function signals in the midcrust and suggested that the shield has reached further west and exists beneath the Altiplano. Our result better defines the shape of the top of the shield as a thrust fault, as was delineated in *Lamb et al*. [1996] based on unpublished oil company data. It is also delineated by the seismicity (yellow dots in Figure 2). A similar image of the underthusting Indian shield beneath the Himalayas is shown in *Schulte-Pelkum et al*. [2005] and *Nelson et al*. [1996]. The shield appears to be absent from the upper mantle structure beneath the Eastern Cordillera because the mantle of the Brazilian Shield lithosphere is likely to have been largely removed in this region by the slab [*O'Driscoll et al*., 2012]. The mantle beneath the sub-Andean shows a high-velocity zone, which we interpret as the shield lithosphere.

### 3.3. The Slab

The dipping slab in the forearc region shows strong signals, with positive and negative pulses delineating the bottom and the top interfaces of the oceanic crust, respectively. From the amplitude of those signals, *Kim and Clayton* [2015] determined the seismic and mineralogical properties of the oceanic crust. They found that compared with the normal subduction segment, an additional 20% reduction in *Vs* exists in the low-velocity layer near the top of the slab, indicating a more fluid-rich layer. Because of the strong hydration of the mantle wedge by the fluids from the slab, the continental Moho signal is weak as the velocity contrast across it is small.

The flat slab signals are not consistently observable in the NW events profile. This is not a problem with the stations, because strong continental Moho signals are observed from this azimuth. The continuous dehydration of the oceanic crust can lead to diminishing slab signals with depth [*Kawakatsu and Watada*, 2007], but this may not be the reason for here since the SE events profile shows strong and consistent slab signals in both primary and multiple phases. We note that the piercing points of the NW events are close to the trajectory of the Nazca Ridge (Figure 1); hence, scattering by the ridge or the hydration and faulting of the crust and uppermost mantle of the oceanic lithosphere during the formation of the ridge may have weakened the slab signals for these events.

The slab becomes flat at ~100 km depth after subducting approximately 200 km from the trench (at 150 km distance in A-A' profile), which is ~20 km deeper compared with the Slab1.0 model [*Hayes et al*., 2012] (Figure 3b). Instead of remaining flat or shallowly dipping down, the slab rises afterward and closely follows the shape of the Moho. In the contact region between the Western and Eastern Cordillera, the Moho warps upward and the flat slab follows this trend (Figure 2) along with the seismicity (Figure S1 of *Dougherty and Clayton* [2014]).

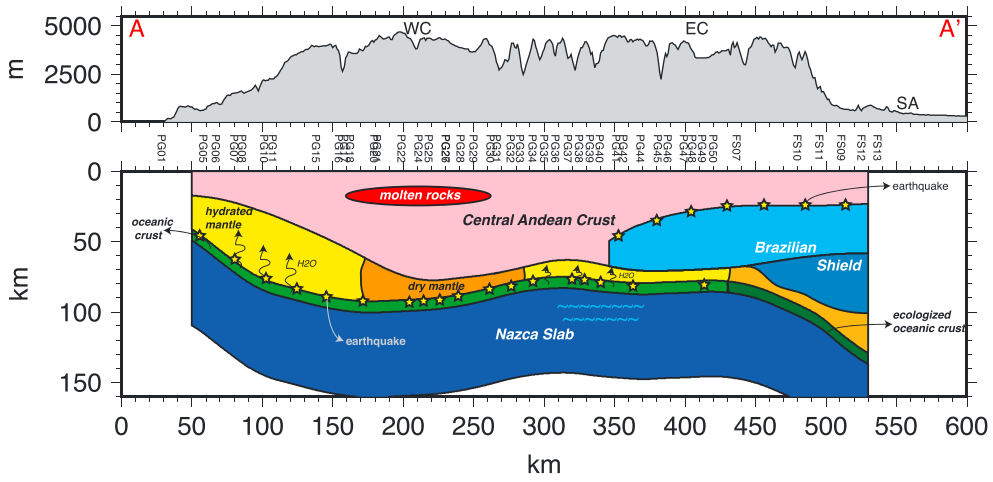


**Figure 4.** Sketch of the structure imaged in this study. The continental and oceanic Moho depths, as well as the top of the Brazilian Shield are based on the SE events profile in Figure 2. The low-velocity zone and mantle wedge velocity contrast are based on Figure 3. The slab lithosphere is assumed to be 80 km thick with an 8 km thick crust. We illustrate the parallel deformation of the slab and the continental Moho above, which indicates a strong suction force between them. The dehydration process is delayed by the flat subduction, and the complete of the dehydration and ecologitization is reflected in the diminishing seismicity.

The seismicity seems to form two clusters centered at 225 km and 325 km distance (Figure S4), where the largest lateral deformation of the slab occurs.

The shape of the flat slab is probably related to the interplate suction force, which can be very large for the flattened slab [*Tovish et al*., 1978]. The mantle is pulled out of the wedge by the subducting slab, and with a small dip angle of the slab, insufficient mantle flows into the wedge, leading to a large negative pressure that further decreases the dip angle of the slab. However, we note that there needs to be some mechanism to raise the slab over some critical angle as in *Tovish et al*. [1978], before the negative pressure can flatten the slab by itself. At angles steeper than the critical angle, the inflow is efficient in decreasing the negative pressure and restoring the slab back to a normal geometry, so that the system is in equilibrium. The subduction of the Nazca Ridge may be the factor that pushes the system beyond the critical angle. This process is much easier with a thick crust and nearby lithospheric root, which obstructs the inflow, and hence enhances the suction force as suggested in *O'Driscoll et al*. [2012].

The initial half (close to the trench) of the flat slab is associated with a high-velocity mantle, which gradually disappears along the slab. The extent of the high velocity is shown in Figure 3a, which is a similar pattern shown to the *Vs* body wave tomography (Figures 13 and 14 in *Young* [2014]). The high *Vs* mantle above the flat slab is also observed in the body wave tomography in the Pampean flat subduction zone in Chile, and is associated with relatively low *Vp*/*Vs* ratio which indicates a cold and dry environment [*Marot et al*., 2014; *Wagner et al*., 2005]. The disappearance of the high-velocity mantle wedge above the flat slab indicates that the slab resumes the dehydration and ecologitization before it steepens again. The ecologitization of the oceanic crust, as is characterized by the vanishing intermediate-depth earthquakes that are due to the dehydration embrittlement [*Jung et al*., 2004], may cause the resteepening of the slab beneath sub-Andean.

## 4. Conclusions

We use a dense linear array to image the structure in the southernmost Peruvian flat subduction zone with receiver functions and surface wave methods. The results are synthesized in Figure 4. The over 4 km high topography of the Central Andes is supported by ~70 km thick crust. An approximately 15 km thick low-velocity zone interpreted as molten rocks is imaged in the upper crust beneath the Western Cordillera. The top of the Brazilian Shield is imaged as a thrust fault beneath the whole Eastern Cordillera. A 10 km shallower Moho is imaged beneath the contact region of the Western and Eastern Cordillera.

The Nazca slab subducts to ~100 km depth and then remains flat for ~300 km distance before it resumes normal subduction. The flat part of the slab closely follows the topography of the continental Moho above,

indicating a strong interplate suction force. The velocity of the upper mantle above the flat slab is comparatively high, indicating a dry and cold environment. The dehydration and ecologitization resumes at 350 km from the trench above the flat slab and lasts for about 100 km until the slab steepens again.

**Acknowledgments**
The PeruSE experiment was supported by the Gordon and Betty Moore Foundation and NSF (EAR-1045683), and the data used are available through IRIS. We thank Lara Wagner and other members of the PULSE experiment for providing data from six stations. We also thank the Editor and reviewers for constructive comments. The script files necessary to reproduce the results are available from the authors upon request.

The Editor thanks Leland O'Driscoll and an anonymous reviewer for their assistance in evaluating this paper.

## References

Antonijevic, S. K., L. S. Wagner, A. Kumar, S. L. Beck, M. D. Long, G. Zandt, H. Tavera, and C. Condori (2015), The role of ridges in the formation and longevity of flat slabs, *Nature*, *524*(7564), 212–215.
Beck, S. L., and G. Zandt (2002), The nature of orogenic crust in the central Andes, *J. Geophys. Res.*, *107*(B10), 2230, doi:10.1029/2000JB000124.
Bishop, B., S. Beck, G. Zandt, A. Kumar, L. Wagner, M. Long, and H. Tavera (2013), Receiver function study of the Peruvian flat-slab region: Initial results from PULSE, paper presented at AGU Fall Meeting Abstracts.
Dorbath, C., M. Granet, G. Poupinet, and C. Martinez (1993), A teleseismic study of the Altiplano and the Eastern Cordillera in northern Bolivia: New constraints on a lithospheric model, *J. Geophys. Res.*, *98*(B6), 9825–9844, doi:10.1029/92JB02406.
Dougherty, S. L., and R. W. Clayton (2014), Seismic structure in southern Peru: Evidence for a smooth contortion between flat and normal subduction of the Nazca Plate, *Geophys. J. Int.*, *200*(1), 534–555.
Eakin, C. M., M. D. Long, S. L. Beck, L. S. Wagner, H. Tavera, and C. Condori (2014), Response of the mantle to flat slab evolution: Insights from local S splitting beneath Peru, *Geophys. Res. Lett.*, *41*, 3438–3446, doi:10.1002/2014GL059943.
Eakin, C. M., M. D. Long, L. S. Wagner, S. L. Beck, and H. Tavera (2015), Upper mantle anisotropy beneath Peru from SKS splitting: Constraints on flat slab dynamics and interaction with the Nazca Ridge, *Earth Planet. Sci. Lett.*, *412*, 152–162.
Gerya, T. V., D. Fossati, C. Cantieni, and D. Seward (2009), Dynamic effects of aseismic ridge subduction: Numerical modelling, *Eur. J. Mineral.*, *21*(3), 649–661.
Gutscher, M.-A. (2002), Andean subduction styles and their effect on thermal structure and interplate coupling, *J. South Am. Earth Sci.*, *15*(1), 3–10.
Hampel, A. (2002), The migration history of the Nazca Ridge along the Peruvian active margin: A re-evaluation, *Earth Planet. Sci. Lett.*, *203*(2), 665–679.
Hayes, G. P., D. J. Wald, and R. L. Johnson (2012), Slab1. 0: A three dimensional model of global subduction zone geometries, *J. Geophys. Res.*, *117*, B01302, doi:10.1029/2011JB008524.
Husson, L., and T. Sempere (2003), Thickening the Altiplano crust by gravity-driven crustal channel flow, *Geophys. Res. Lett.*, *30*(5), 1243, doi:10.1029/2002GL016877.
Jung, H., H. W. Green Ii, and L. F. Dobrzhinetskaya (2004), Intermediate-depth earthquake faulting by dehydration embrittlement with negative volume change, *Nature*, *428*(6982), 545–549.
Kawakatsu, H., and S. Watada (2007), Seismic evidence for deep-water transportation in the mantle, *Science*, *316*(5830), 1468–1471.
Kennett, B. N., and E. Engdahl (1991), Traveltimes for global earthquake location and phase identification, *Geophys. J. Int.*, *105*(2), 429–465.
Kikuchi, M., and H. Kanamori (1982), Inversion of complex body waves, *Bull. Seismol. Soc. Am.*, *72*(2), 491–506.
Kim, Y., and R. W. Clayton (2015), Seismic properties of the Nazca oceanic crust in southern Peruvian subduction system, *Earth Planet. Sci. Lett.*, doi:10.1016/j.epsl.2015.07.055.
Lamb, S., L. Hoke, L. Kennan, and J. Dewey (1996), Cenozoic evolution of the Central Andes in Bolivia and northern Chile, *Geol. Soc. London Spec. Publ.*, *121*, 237–264.
Ligorría, J. P., and C. J. Ammon (1999), Iterative deconvolution and receiver-function estimation, *Bull. Seismol. Soc. Am.*, *89*(5), 1395–1400.
Linkimer, L., S. L. Beck, S. Y. Schwartz, G. Zandt, and V. Levin (2010), Nature of crustal terranes and the Moho in northern Costa Rica from receiver function analysis, *Geochem. Geophys. Geosyst.*, *11*, Q01S19, doi:10.1029/2009GC002795.
Ma, Y., and R. W. Clayton (2014), The crust and uppermost mantle structure of Southern Peru from ambient noise and earthquake surface wave analysis, *Earth Planet. Sci. Lett.*, *395*, 61–70.
Mamani, M., G. Wörner, and T. Sempere (2010), Geochemical variations in igneous rocks of the Central Andean orocline (13 S to 18 S): Tracing crustal thickening and magma generation through time and space, *Geol. Soc. Am. Bull.*, *122*(1–2), 162–182.
Manea, V. C., M. Pérez-Gussinyé, and M. Manea (2012), Chilean flat slab subduction controlled by overriding plate thickness and trench rollback, *Geology*, *40*(1), 35–38.
Marot, M., T. Monfret, M. Gerbault, G. Nolet, G. Ranalli, and M. Pardo (2014), Flat versus normal subduction zones: A comparison based on 3-D regional traveltime tomography and petrological modelling of central Chile and western Argentina (29°–35°S), *Geophys. J. Int.*, *199*(3), 1633–1654.
McQuarrie, N., B. K. Horton, G. Zandt, S. Beck, and P. G. DeCelles (2005), Lithospheric evolution of the Andean fold-thrust belt, Bolivia, and the origin of the central Andean plateau, *Tectonophysics*, *399*(1), 15–37.
Myers, S. C., S. Beck, G. Zandt, and T. Wallace (1998), Lithospheric-scale structure across the Bolivian Andes from tomographic images of velocity and attenuation for P and S waves, *J. Geophys. Res.*, *103*(B9), 21,233–21,252, doi:10.1029/98JB00956.
Nelson, K. D., W. Zhao, L. Brown, J. Kuo, J. Che, X. Liu, S. Klemperer, Y. Makovsky, R. Meissner, and J. Mechie (1996), Partially molten middle crust beneath southern Tibet: Synthesis of project INDEPTH results, *Science*, *274*(5293), 1684–1688.
O'Driscoll, L. J., M. A. Richards, and E. D. Humphreys (2012), Nazca-South America interactions and the late Eocene-late Oligocene flat slab episode in the central Andes, *Tectonics*, *31*, TC2013, doi:10.1029/2011TC003036.
Oncken, O., D. Hindle, J. Kley, K. Elger, P. Victor, and K. Schemmann (2006), Deformation of the central Andean upper plate system—Facts, fiction, and constraints for plateau models, in *The Andes*, edited by O. Oncken et al., pp. 3–27, Springer, Berlin.
PeruSE (2013), Peru subduction experiment, *Caltech. Dataset.*, doi:10.7909/C3H41PBZ.
Phillips, K., and R. W. Clayton (2014), Structure of the subduction transition region from seismic array data in southern Peru, *Geophys. J. Int.*, *196*, 1889–1905.
Phillips, K., R. W. Clayton, P. Davis, H. Tavera, R. Guy, S. Skinner, I. Stubailo, L. Audin, and V. Aguilar (2012), Structure of the subduction system in southern Peru from seismic array data, *J. Geophys. Res.*, *117*, B11306, doi:10.1029/2012JB009540.
Ramos, V. A., and A. Folguera (2009), Andean flat-slab subduction through time, *Geol. Soc. London Spec. Publ.*, *327*(1), 31–54.
Schilling, F. R., R. B. Trumbull, H. Brasse, C. Haberland, G. Asch, D. Bruhn, K. Mai, V. Haak, P. Giese, and M. Muñoz (2006), Partial melting in the Central Andean crust: A review of geophysical, petrophysical, and petrologic evidence, in *The Andes*, edited by O. Oncken et al., pp. 459–474, Springer, Berlin.
Schulte-Pelkum, V., G. Monsalve, A. Sheehan, M. Pandey, S. Sapkota, R. Bilham, and F. Wu (2005), Imaging the Indian subcontinent beneath the Himalaya, *Nature*, *435*(7046), 1222–1225.

Skinner, S. M., and R. W. Clayton (2013), The lack of correlation between flat slabs and bathymetric impactors in South America, *Earth Planet. Sci. Lett.*, *371–372*, 1–5.

Tassara, A. (2005), Interaction between the Nazca and South American plates and formation of the Altiplano-Puna plateau: Review of a flexural analysis along the Andean margin (15–34 S), *Tectonophysics*, *399*(1), 39–57.

Tovish, A., G. Schubert, and B. P. Luyendyk (1978), Mantle flow pressure and the angle of subduction: Non Newtonian corner flows, *J. Geophys. Res.*, *83*(B12), 5892–5898, doi:10.1029/JB083iB12p05892.

Trumbull, R. B., U. Riller, O. Oncken, E. Scheuber, K. Munier, and F. Hongn (2006), The time-space distribution of Cenozoic volcanism in the South-Central Andes: A new data compilation and some tectonic implications, in *The Andes*, edited by O. Oncken, pp. 29–43, Springer, Berlin.

van Hunen, J., A. P. van den Berg, and N. J. Vlaar (2002), The impact of the South American plate motion and the Nazca Ridge subduction on the flat subduction below South Peru, *Geophys. Res. Lett.*, *29*(14), 35–31–35–34, doi:10.1029/2001GL014004.

van Hunen, J., A. P. van den Berg, and N. J. Vlaar (2004), Various mechanisms to induce present-day shallow flat subduction and implications for the younger Earth: A numerical parameter study, *Phys. Earth Planet. Inter.*, *146*(1), 179–194.

Wagner, L., S. Beck, and G. Zandt (2005), Upper mantle structure in the south central Chilean subduction zone (30 to 36 S), *J. Geophys. Res.*, *110*, B01308, doi:10.1029/2004JB003238.

Ward, K. M., R. C. Porter, G. Zandt, S. L. Beck, L. S. Wagner, E. Minaya, and H. Tavera (2013), Ambient noise tomography across the Central Andes, *Geophys. J. Int.*, *194*(3), 1559–1573.

Yang, Y., M. Liu, and S. Stein (2003), A 3-D geodynamic model of lateral crustal flow during Andean mountain building, *Geophys. Res. Lett.*, *30*(21), 2093, doi:10.1029/2003GL018308.

Young, B. E. (2014), Regional body-wave tomography of the Peruvian flat slab, Univ. of North Carolina at Chapel Hill.

Yuan, X., S. Sobolev, R. Kind, O. Oncken, G. Bock, G. Asch, B. Schurr, F. Graeber, A. Rudloff, and W. Hanka (2000), Subduction and collision processes in the Central Andes constrained by converted seismic phases, *Nature*, *408*(6815), 958–961.

Zhu, L., and H. Kanamori (2000), Moho depth variation in southern California from teleseismic receiver functions, *J. Geophys. Res.*, *105*(B2), 2969–2980, doi:10.1029/1999JB900322.